Integrated phased array for wide-angle beam steering

Ami Yaacobi,[1] Jie Sun,[1] Michele Moresco,[1] Gerald Leake,[2] Douglas Coolbaugh,[2] and Michael R. Watts[1,*]

[1]*Research Laboratory of Electronics, Massachusetts Institute of Technology, Cambridge, Massachusetts 02139, USA*

[2]*College of Nanoscale Science and Engineering, University at Albany, Albany, New York 12203, USA*

**Corresponding author: mwatts@mit.edu*

Received April 25, 2014; revised June 26, 2014; accepted June 26, 2014;
posted June 30, 2014 (Doc. ID 210876); published July 30, 2014

We demonstrate an on-chip optical phased array fabricated in a CMOS compatible process with continuous, fast (100 kHz), wide-angle (51°) beam-steering suitable for applications such as low-cost LIDAR systems. The device demonstrates the largest (51°) beam-steering and beam-spacing to date while providing the ability to steer continuously over the entire range. Continuous steering is enabled by a cascaded phase shifting architecture utilizing, low power and small footprint, thermo-optic phase shifters. We demonstrate these results in the telecom C-band, but the same design can easily be adjusted for any wavelength between 1.2 and 3.5 μm.

OCIS codes: (140.3300) Laser beam shaping; (110.5100) Phased-array imaging systems; (010.3640) Lidar.
http://dx.doi.org/10.1364/OL.39.004575

On-chip optical phased arrays have been widely investigated in the last few years [1–4] for applications in many fields including holographic video displays, optical communication systems, and low cost light detection and ranging (LIDAR) systems. In particular, low cost chip-scale LIDAR can, in principle, dramatically enhance accident avoidance systems in the automotive industry [5–8]. However, LIDAR systems used for autonomous vehicles, to date, have been extremely expensive, in some cases exceeding the cost of the car itself or any other component used for its autonomous functionality [8]. Moreover, these mechanically steered LIDAR systems do not possess a form factor that fits well within a modern automobile. By contrast, chip-scale LIDAR systems can be both low-cost and compact, and are, therefore, important components for commercial autonomous vehicles in the future.

Yet, automotive applications impose constraints that are challenging for on-chip phased arrays. While two-dimensional beam steering is usually not required, high-speed continuous beam steering is often necessary. Architectures mentioned in [1–3,9,10] utilize lookup tables to determine the required signal for every beam angle. For continuous steering in such systems, a delay is required for the phase shifters to stabilize at every step of the sweep, substantially increasing the time of the sweep by the product of the number of angular steps required and the associated relaxation time for each step in the angle. With the architecture given in [11], such a delay is not required, but the power needed for steering increases as the square of the number of antennas increases, thereby restricting the scaling of the array. More importantly, for efficient, large-angle, and low crosstalk operation, a large angle between the different optical orders is necessary. Despite the substantial progress in optical phased arrays current systems can only steer across a maximum of ∼24° [2], whereas, autonomous vehicle applications typically require scan angles exceeding 45°.

Here we demonstrate a high-speed, low-power, and wide-scan-angle optical phased array. The array is based on a novel phase shifting architecture. The approach utilizes 32 μm long grating based antennas, fed through evanescent field waveguide couplers from a bus waveguide with directly integrated thermo-optic phase shifters [12,13]. The demonstrated phased array is continuously steerable over a 51° angular range with a 10.6 V signal, an average power consumption of ∼18 mW/antenna, and a 3 dB cutoff speed of 100 kHz. We operate this array at the eye-safe 1550 nm wavelength, but the design can easily be converted to work at any wavelength between 1.2 and 3.5 μm allowing for tens of thousands of LIDAR systems to work together without interfering, an important feature for accident avoidance applications.

As stated above, when designing an optical phased array, pushing the side lobes (or orders) farther apart is extremely important. Side lobes radiate power in undesired directions that would otherwise go to the main beam and therein increase the probability of crosstalk between different ports while reducing the gain of the phased array antenna. The presence of side lobes also indicates a narrowed steering angle since there is no benefit in steering beyond the spacing of two consecutive beams. We define the beam spacing, $\Delta\phi$, as the angle between the fundamental (emitting straight forward) and the next order lobes. This angle can be derived by applying the first-order constructive-interference condition on the array's antennas with all of the antennas emitting at the same phase, and it is related to the antenna pitch, d, by

$$\sin(\Delta\phi) = \frac{\lambda}{d}, \tag{1}$$

where λ is the laser wavelength. Thus, increasing the angle between two consecutive lobes requires narrowing the antenna spacing. Unfortunately, since the antenna spacing needs to approach a half-wavelength to achieve the full 180° steering range, approaching this range, prevents other components from existing between the antennas (e.g., preventing phase shifters as in [1], and/or waveguides to different antennas as in [14]). Given that silicon photonics is inherently two-dimensional, extracting other components from between the antennas limits the array to one dimensional electrical steering and forces long optical antennas to cover the necessary aperture size. In the longitudinal direction, i.e., along the

antenna waveguides, the emission angle of the N^{th} order θ_N, in air, is given by [15]

$$\sin(\theta_N) = n_{\text{eff}} - \frac{N\lambda}{\Lambda}, \tag{2}$$

where n_{eff} is the waveguide effective index and Λ is the grating period. Since, in our case, $\lambda/\Lambda = n_{\text{eff}} > 1$ only the first-order exists in the longitudinal direction [see Fig 1(a) for angles].

The antenna gratings were designed using a shallow etch on the sides of the waveguide. In this manner, the interleaving of shallow etched and fully etched silicon regions can be controlled very accurately enabling infinitesimal perturbations to be imposed at the antenna input and continuously stronger perturbations as light propagates deeper in the antenna so as to ensure uniform emission from the decaying field. As a result, the forward/backward symmetry of the antenna is also broken allowing for higher coupling efficiency between the waveguide propagating mode and the emitted free space mode. Unfortunately the up/down symmetry in our design is not efficiently broken and finite-difference time-domain (FDTD) simulations show that about half of the light emissions in the downward direction. Considering this and power loss to side lobes we estimate the total efficiency to be ~25%. FDTD simulations were also used to determine the grating strength and the pitch along the emitter. The grating strength was adjusted to ensure uniform intensity of emission along the antenna length, whereas grating pitch was tuned, for each strength, to minimize aberrations and ensure a collimated beam. Figure 1(a) is a simulation image showing a section of the antenna tested between its two sequential antennas with its flux monitors for up/down emission, transmission, and reflection. These FDTD simulations also reveal minimal coupling between adjacent antennas even when antenna waveguides are placed as close as 1 μm apart (1.4 μm in pitch).

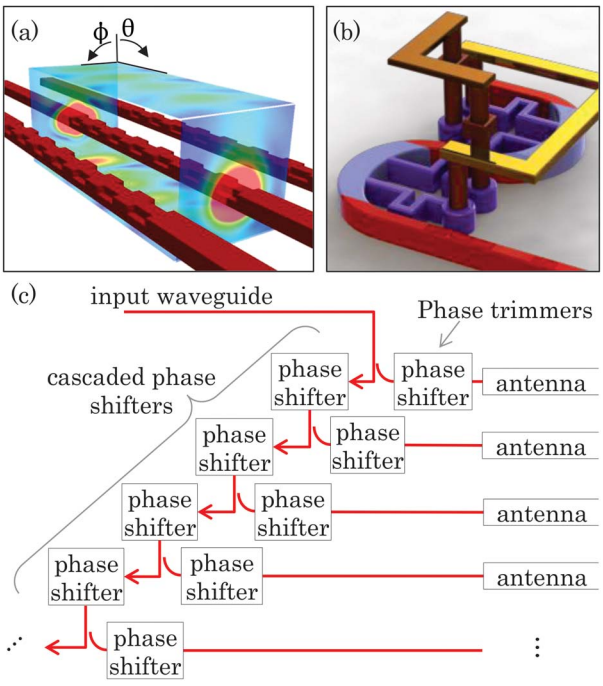

Fig. 1. Design: (a) A finite-difference time-domain (FDTD) simulation of a small section of the emitters showing the flux monitors used for calculating the amount of power extracted from the waveguide per unit length. An illustration of lateral, ϕ, and longitudinal, θ, angles is added at the top. (b) A schematic of the phase shifter showing the intrinsic waveguide (red), the lightly doped heater (blue), the high doped Si wires contacting the heater (purple) and the metals and contacts (gold/brown). (c) The architecture of the phased array showing the cascaded phase shifting drawn compatibly with Fig. 2(a). The red lines show the waveguide paths and the redundant phase trimmers were drawn to illustrate the components shown in Fig. 2(a).

Phase shifting is achieved using the thermo-optic effect in silicon in which a part of the waveguide was doped to form a resistive heater. To achieve electrical contact to the heater elements integrated in the waveguide, we use an S-shaped adiabatic bend, broadening the waveguide from 400 nm to 1 μm width in the middle of each curve and back to 400 nm. This type of bending and broadening pushes the mode away from the inner part of the curve, allowing electrical contacts to be made with minimal scattering losses [12,13]. Such an S-shape structure also allows for a larger phase shift in a small footprint. Additionally, the use of highly doped, zigzagged, silicon lines enables electrical contacting to the waveguide without melting the metal-to-Si contacts at the waveguide's high temperatures. Figure 1(b) shows the phase shifter design where intrinsic, low, and high doping levels are shown as red, blue, and purple, respectively. Comsol simulations show that the high temperature shift applies not only to the doped volume, but flows quickly along the waveguide, thus enabling larger phase shifts. Finally, by directly heating the waveguide, which has a small volume and low heat capacity, we are able to reduce the total heating energy required for a given phase shift thus allowing for more efficient, high-speed phase shifting. Reference [12] shows a single phase shifter of this type to have a time constant of $\tau \sim 2.3$ μs limits the 3 dB cutoff frequency of this phase shifter $f_{3\text{ dB}}$ to be about 110 kHz. For this bandwidth we use $f_{3\text{ dB}} = \sqrt{3}/(2\pi\tau)$ rather than the conventional, power, 3 dB cutoff $f_{3\text{ dB}} = 1/(2\pi\tau)$ since the phase response is not squared.

The cascaded phase shifting architecture shown in Fig. 1(c) enables continuous steering using one input signal. By driving all of the cascaded phase shifters with the same voltage, a constant phase difference between consecutive antennas is developed, enabling continuous steering. This is different from earlier designs mentioned above. In contrast to [1–3,9,10], since in the cascaded phase shifting architecture an electric power signal is linearly translated to the beam angle, the cutoff steering frequency is equal to the phase shifter cutoff frequency allowing for high-speed steering. Compared to the architecture shown in [11] our design, regardless of the size of the array, requires equal power for all antennas and is easily scalable to larger arrays. As a consequence, the cascaded phase shifting architecture enables continuous and high-speed steering with low power consumption.

The array was fabricated in a 300 mm CMOS compatible foundry using 193 nm optical immersion lithography on a silicon-on-insulator wafer with $\sim 1 \times 10^{15}$ cm^{-3} p-type, 220 nm thick, silicon on a 2 μm thick buried oxide.

The process included a deep (220 nm) etch and a shallow (110 nm) etch to define the silicon layer, low (2×10^{18} cm^{-3}) and high ($\sim 10^{20}$ cm^{-3}) n-type doping levels, two layers of copper metal interconnect and their via contacts to the silicon layer. The phased-array structure was formed by combining the aforementioned components in such a way that the antenna spacing is minimized, and thus the beam spacing is maximized. Placing sixteen, 32 μm long grating-based antennas described earlier, with a 2 μm pitch, a 32 μm × 32 μm array was created. A scanning electron microscope (SEM) image of the fabricated array can be seen in Fig. 2(a) while the inset shows how the phase shifters are integrated in the cascaded architecture. A close-up on the individual phase shifter can be seen in the false-colored SEM in Fig. 2(b) showing its different doping levels as red, blue, and purple representing intrinsic, medium, and high doping levels, respectively. An optical path with a length of ~1.5 μm, average width of ~0.75 μm, and thickness of 0.22 μm, medium doped, yields a total resistance of ~6.2 kΩ per curve. The two curves, connected in parallel in each phase-shifter create heating of around 500°C and change the Si refractive index by ~3.2% [16] with 10.6 V applied. Figure 2(c) shows two close-up views of the gratings, at the beginning and end of one antenna, demonstrating the weak and strong perturbations mentioned above, respectively. In agreement to Eq. (1), a 51° beam spacing in the lateral dimension was achieved and in agreement with Eq. (2) no additional beams were observed in the longitudinal direction.

The far field spot size full width at half-maximum (FWHM) was measured to be ~3.3°, which is the diffraction limit for a 32 μm rectangular aperture. To characterize the steering, a uniform voltage was applied across all the cascaded phase shifters (no voltage was necessary on any of the phase trimmers). Figure 3(a) shows the resulting far field beam, captured with an InGaAs near infrared (NIR) camera, as it is steered over the whole beam spacing. The images were taken through a NA = 0.4 lens.

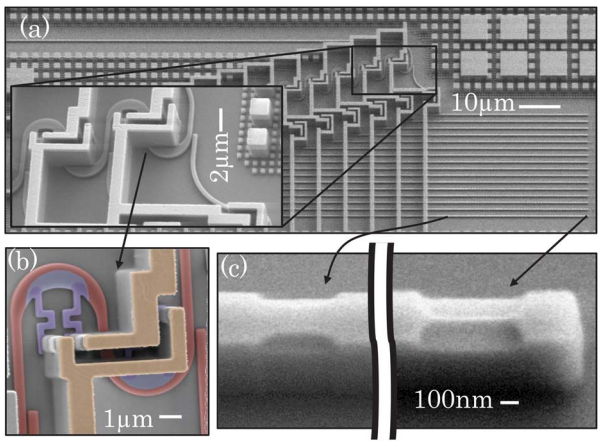

Fig. 2. Fabrication: (a) A SEM image of the array showing the whole device and another SEM image (inset) magnifying the first two cascaded phase shifters. (b) A false-colored SEM of a single phase shifter illustrating the intrinsic waveguide (red), low doped resistor (blue), and high doped Si wires (purple). (c) SEM images of the first and last antenna gratings showing the difference in grating strength along the emitter. All SEM images were taken after removing the SiO_2 cladding.

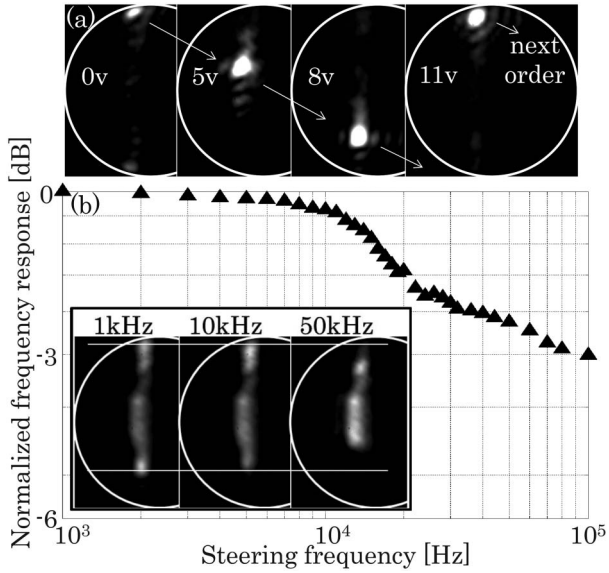

Fig. 3. (a) Far field images of slow steering show steering throughout the whole beam spacing. (b) Normalized frequency response of the phased array showing the 3 dB level at ~100 kHz with the inset illustrating the method we used to measure that frequency response. It shows actual, high-speed, steering images at different frequencies and proves how the amplitude decreases with frequency. The white circles in the images show the 0.4 numerical aperture of the imaging system (24° in radius).

This lens shows an angular radius of only 24° and, therefore, cannot show more than one beam at a time. However, it can still clearly be seen that at 11 V the next order shows up at the same position where the main beam was at 0 V bias, which confirms that a 2π phase shift was achieved.

In order to measure the frequency response of the system, a sinusoidal input steering voltage, with frequencies much higher than the inverse integration time of the NIR camera, was applied. Such an input signal enabled us to see the steering as a steady line where the steering amplitude is indicated by half the line length. The inset of Fig. 3(b) shows example images at 1, 10, and 50 kHz and how the steering angle reduces with frequency. The normalized frequency response of the array was measured by comparing the steering angle with the steering angle at low frequencies. Figure 3(b) shows the normalized steering amplitude as a function of steering frequency. The 3 dB cutoff operation frequency for continuous steering was found to be ~100 kHz and the maximal steering speed up to 5×10^6 deg/s.

In conclusion, we demonstrate a high-speed silicon photonic optical phased array with, to the best of our knowledge, the widest scanning range (51°) achieved to date. This one-dimensional phased-array provides continuous, high-speed beam steering suitable for LIDAR applications. In the longitudinal dimension, several arrays can be implemented on the same chip with different grating periods in order to generate several scanning plains. This method of repeating emitters in order to generate 2-D scanning is common in LIDAR systems (e.g., Velodyne LIDAR HDL-64E [17]). Nevertheless, [2,14] suggest longitudinal steering by sweeping the wavelength.

This is possible but also points to another method that can be applied; by driving this phased array with a spectral comb multiple beams can be emitted simultaneously to achieve 2-D scanning. The design can be easily modified for different wavelengths within the 1.2–3.5 μm range. More importantly, this phased array was fabricated in a standard 300 mm CMOS fabrication facility using a custom silicon photonics process. As such, the device can be cost-effectively mass produced to serve numerous applications including automotive accident avoidance technologies.

This work was supported by Toyota Central R&D Labs., Inc. (TCRDL) and by the Defense Advanced Research Projects Agency (DARPA) Microsystems Technology Office's (MTO) EPHI program, grant no. HR0011-12-2-0007. We would like to thank Cheryl Sorace-Agaskar, Dr. Ehsan S. Hosseini, Erman Timurdogan of MIT and Tsuyoshi Nomura of TCRDL for helpful discussions.

References

1. J. Sun, E. Timurdogan, A. Yaacobi, E. S. Hosseini, and M. R. Watts, Nature **493**, 195 (2013).
2. J. C. Hulme, J. K. Doylend, M. J. R. Heck, J. D. Peters, M. L. Davenport, J. T. Bovington, L. A. Coldren, and J. E. Bowers, Proc. SPIE **8989**, 898907 (2014).
3. B. W. Yoo, T. Chan, M. Megens, T. Sun, W. Yang, Y. Rao, D. A. Horsley, C. J. Chang-Hasnain, and M. C. Wu, Proc. SPIE **8633**, 86330F (2013).
4. C. T. DeRose, R. D. Kekatpure, D. C. Trotter, A. Starbuck, J. R. Wendt, A. Yaacobi, M. R. Watts, U. Chettiar, N. Engheta, and P. S. Davids, Opt. Express **21**, 5198 (2013).
5. K. Takagi, K. Morikawa, T. Ogawa, and M. Saburi, in *Intelligent Vehicles Symposium* (IEEE, 2006), pp. 120–125.
6. J. Levinson, J. Askeland, J. Becker, J. Dolson, D. Held, S. Kammel, J. Z. Kolter, D. Langer, O. Pink, V. Pratt, M. Sokolsky, G. Stanek, D. Stavens, A. Teichman, M. Werling, and S. Thrun, in *Fourth Intelligent Vehicles Symposium* (IEEE, 2011), pp. 163—168.
7. T. Luettel, M. Himmelsbach, and H. J. Wuensche, Proc. IEEE **100**, 1831 (2012).
8. A. Fisher, Popular Sci. **18** (2013).
9. D. Kwong, A. Hosseini, J. Covey, Y. Zhang, X. Xu, H. Subbaraman, and R. T. Chen, Opt. Lett. **39**, 941 (2014).
10. W. Guo, P. Binetti, C. Althouse, M. Masanovic, H. Ambrosius, L. Johansson, and L. Coldren, IEEE J. Sel. Top. Quantum Electron. **19**, 8500508 (2013).
11. K. V. Acoleyen, W. Bogaerts, J. Jágerská, N. L. Thomas, R. Houdré, and R. Baets, Opt. Lett. **34**, 1477 (2009).
12. M. R. Watts, J. Sun, C. DeRose, D. C. Trotter, R. W. Young, and G. N. Nielson, Opt. Lett. **38**, 733 (2013).
13. M. R. Watts, Opt. Lett. **35**, 3231 (2010).
14. K. V. Acoleyen, H. Rogier, and R. Baets, Opt. Express **18**, 13655 (2010).
15. R. Waldhäusl, B. Schnabel, P. Dannberg, E. B. Kley, A. Bräuer, and W. Karthe, Appl. Opt. **36**, 9383 (1997).
16. H. H. Li, J. Phys. Chem. Ref. Data **9**, 561 (1980).
17. HDL-64E in Velodyne Website, http://velodynelidar.com/lidar/hdlproducts/hdl64e.aspx.